Nanoscale

ROYAL SOCIETY OF CHEMISTRY

PAPER

View Article Online
View Journal | View Issue

Cite this: *Nanoscale*, 2022, **14**, 17003

Core–satellite–satellite hierarchical nanostructures: assembly, plasmon coupling, and gap-selective surface-enhanced Raman scattering†

Hoa Duc Trinh, Seokheon Kim, Joohwan Park and Sangwoon Yoon *

The plasmonic properties of gold nanoparticles (AuNPs), such as color tunability, electric field generation, hot carrier generation, and localized heating, are significantly enhanced in the nanogaps between AuNPs. Therefore, the creation and control of nanogaps are key to developing advanced plasmonic nanomaterials. Most AuNP nanoassemblies, including dimers, trimers, and core–satellites, have a single type of nanogap within the assembly. In this study, we construct core–satellite–satellite (CSS) hierarchical, fractal-like nanostructures featuring two types of nanogaps, namely first generation nanogaps (Gap1) between the core and first satellite (Sat1) AuNPs and second generation nanogaps (Gap2) between Sat1 and second satellite (Sat2) AuNPs. The sequential and alternating immersion of glass slides in different-sized AuNPs and linkers forms CSS with perfect yield. The UV-vis spectroscopy, combined with charge density distribution calculations, reveals the nature of the plasmon coupling between the AuNPs that constitute CSS nanoassemblies. The plasmon coupling can be tuned by independently varying Gap1 and Gap2. Furthermore, we explore the electric field amplification in Gap1 and Gap2 by comparing the surface-enhanced Raman scattering signal intensity selectively from each nanogap. This new type of nanostructure provides a great flexibility to control and enhance the plasmonic properties of noble metal nanoparticles.

Received 23rd August 2022,
Accepted 5th November 2022

DOI: 10.1039/d2nr04621k

rsc.li/nanoscale

Introduction

Noble metal nanoparticles are versatile materials with a wide variety of applications.[1–4] Most representative properties of noble metal nanoparticles, such as bright visible colors, electric field generation around the nanoparticles, highly energetic charge carrier generation, and localized heating, originate from the collective oscillation of conduction electrons in the nanoparticles, called plasmons.[5] Such plasmonic properties are used in sensors,[6–9] imaging,[10–12] surface-enhanced spectroscopy,[13] photocatalysis,[14–19] and nanoscale heating.[3,20–24]

The nanogaps between nanoparticles significantly strengthens the plasmonic properties. The color of nanoparticles is tunable across the visible wavelength region as the nanogap distance varies.[25–27] The electric field is more intensified in nanogaps through the capacitive effect,[28,29] which is responsible for surface-enhanced Raman scattering (SERS).[13,30,31] Nanogaps promote the generation of hot charge carriers, thereby enabling a reaction that is unfeasible without the nanoparticles.[32–36] Plasmonic heating further increases the temperature in the nanogaps.[21,24,37] Thus, nanogaps play a crucial role in plasmonics. Accordingly, creating and controlling nanogaps is one of the main themes in this research field.

One of the best approaches for creating nanogaps is the formation of nanoparticle assemblies. When nanoparticles are brought together, nanogaps are naturally formed between the nanoparticles. Various nanoassembly structures have been developed. We categorize the assemblies according to the nanoparticle type (namely, component) that comprises the assembly. For similar-sized spherical nanoparticles (one-component systems), the easily conceivable structures include dimers,[38–46] trimers,[45,47–53] tetramers,[54] oligomers,[55–58] and their geometric isomers as the number of constituent nanoparticles increases. For two different-sized nanoparticles (two-component systems), the assemblies evolve from heterodimers[59,60] to core–satellite ("CS") structures, where central core nanoparticles are surrounded by smaller satellite

Department of Chemistry, Chung-Ang University, 84 Heukseok-ro, Dongjak-gu, Seoul 06974, Korea. E-mail: sangwoon@cau.ac.kr

†Electronic supplementary information (ESI) available: Detailed experimental and simulation methods, characterization data of the AuNPs used in the experiments, a gallery of SEM images of the CSS that were prepared using various linker combinations, a comparison between the perfect radiant coupling mode and *Di–Di–Di* coupling mode, data that shows the difference in the binding forces between electrostatic interaction and covalent bonding, a comparison of the SERS intensity between ABT and C8DT, calculated scattering spectra and electric field distribution of CS and CSS at resonance wavelengths (PDF). See DOI: https://doi.org/10.1039/d2nr04621k

nanoparticles.[61–71] The controlled high-yield assembly of any one- or two-component nanoparticles is challenging. Thus, the experimental realization and its outcome would be truly a great accomplishment. However, in these nanoassemblies only one type of nanogap exists regardless of the number of constitutive nanoparticles, limiting the degrees of freedom that can be explored. For example, two nanogaps have identical characteristics in trimers because the same type of nanoparticle defines each nanogap. The nanogaps in CS nanoassemblies are simply multiples of heterodimers.

This study aims to realize nanogaps with two different characteristics in one nanoassembly unit. The combination of these nanogaps diversifies the plasmonic properties. Additional plasmon coupling from secondary nanogaps is expected to expand the optical resonance and consequently, enables color tuning in a wider range. Furthermore, a comparison of the two different nanogaps for amplifying electric fields will provide a valuable guideline for designing sensitive SERS materials. The contribution of additional nanogaps to hot carrier generation efficiency or local heating remains to be explored.

Here, we construct three-component hierarchical nanoassembly structures where two generations of assemblies are sequentially established to form their own nanogaps. More specifically, large-size gold nanoparticles ("Core" AuNPs) are adsorbed on a glass slide. Then, mid-sized AuNPs are attached to the Core (first generation satellites, "Sat1"). Finally, other smaller-sized AuNPs decorate each Sat1 AuNP (second generation satellites, "Sat2"), completing the core–satellite–satellite ("CSS") nanoassemblies. We also investigate the plasmon coupling and electric field interactions within the CSS nanoassemblies.

Results and discussion

Assembly method

We adopted the sequential adsorption method on glass slides to assemble nanoparticles (Fig. 1).[38] The experimental details are provided in the ESI.† Briefly, we prepared citrate-stabilized AuNPs with three different sizes (70 ± 8, 32 ± 4, and 20 ± 2 nm) for use as the Core, Sat1, and Sat2 nanoparticles, respectively (Fig. S1†). The assembly proceeds as follows: (1) glass slides (25 × 13 mm^2) are thoroughly cleaned and amine-functionalized using (3-aminopropyl)trimethoxysilane (APTMS); (2) the amine-coated glass slide is immersed in the 70 nm AuNP solution (23 pM, 5 mL) for 5 h to anchor the Core AuNPs onto the glass slide; (3) after washing, the AuNP/glass slide is immersed in a NaOH solution (50 mM, 5 mL) for 5 h to remove the free APTMS on the glass slide. This so-called masked desilanization prohibits other citrate-capped AuNPs, such as Sat1 and Sat2, from adsorbing on the glass slide in later steps;[38] (4) the Core/glass slide is then immersed in an ethanol solution of "Linker1" molecules (1 mM, 5 mL) for 1 h to attach the linkers to the Core AuNP surfaces in a self-assembled monolayer (SAM) formation.[72] This step uses dithiol or aminothiol molecules, including 1,8-octanedithiol (C8DT), 1,4-benzenedimethanethiol (BDMT), and 4-aminobenzenethiol (ABT); (5) immersion in a citrate-capped Sat1 AuNP solution (32 nm, 214 pM, 5 mL) for 6 h forms CS nanoassemblies on the glass slide; (6) another immersion step in a "Linker2" solution (1 mM, 5 mL) for 1 h replaces the weakly bound citrates on the Sat1 AuNPs with Linker2 molecules; and (7) subsequent immersion into a solution of 20 nm Sat2 AuNPs (710 pM, 5 mL) for 4 h completes the formation of CSS nanoassemblies. Notably, without the masked desilanization process (step (3)), Sat1 and Sat2 AuNPs would adsorb onto the amine-coated glass slides, thereby lowering the yield of the CS or CSS nanoassemblies.

Structural and optical characteristics

Fig. 2 shows the structural and optical properties of the prepared CSS nanoassemblies. The representative scanning electron microscopy (SEM) image in Fig. 2a shows the successful assembly of CSS hierarchical nanostructures. Addtional SEM images of the CSS nanoassemblies with various linkers are available in Fig. S2.† The images show that our assembly method is extremely reproducible. No individual or partly

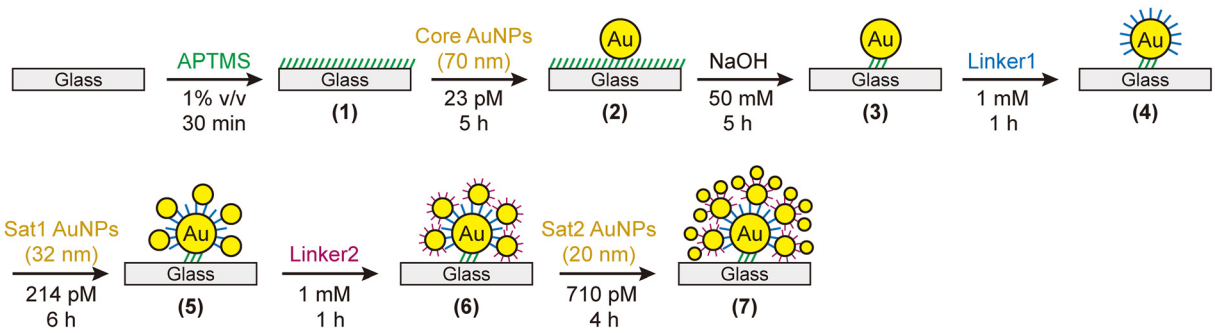

Fig. 1 Stepwise assembly scheme for CSS. (1) A clean glass slide is amine-coated using APTMS. (2) Citrate-stabilized Core AuNPs (70 nm) adsorb on the glass slide through electrostatic interactions. (3) Unbound amines on the glass slide are removed by NaOH (masked desilanization process). (4) Dithiol or aminothiol linkers (Linker1) replace citrates on the Core AuNP and functionalize the surface with thiol or amine. (5) Citrate-capped Sat1 AuNPs (32 nm) attach to the Linker1 on the Core AuNP to form a CS nanoassembly. (6) Linker2 molecules bind to the Sat1 AuNP surfaces, displacing the citrates. (7) Citrate-capped Sat2 AuNPs (20 nm) adsorb on the Linker2, completing the formation of CSS.

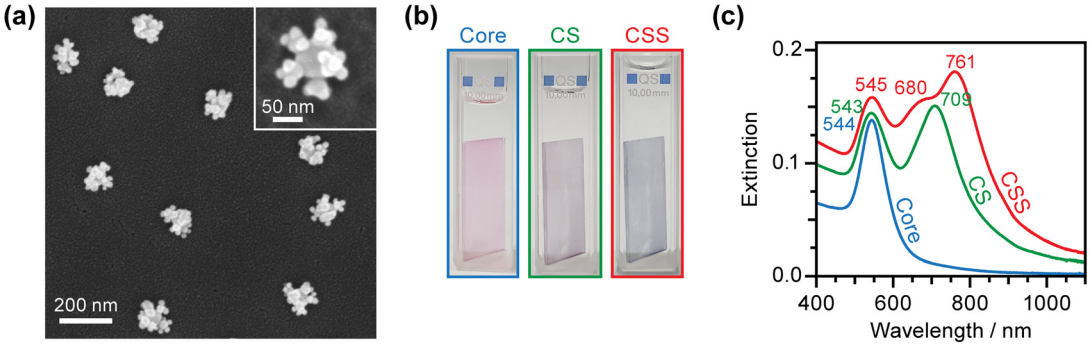

Fig. 2 Structural and optical characteristics of CSS nanoassemblies. (a) Representative SEM image (inset: a magnified view) of CSS nanoassemblies with C8DT as linkers. (b) Photographic images and (c) UV-vis spectra of the Core, CS, and CSS with C8DT as linkers.

assembled AuNPs are observed, indicating that all the nanoparticles prepared on the glass slides are CSS nanoassemblies (perfect yield). Analysis of the SEM images (N = 68) indicates that, on average, eight CSS nanoassemblies are formed within a 1 μm^2 area. Thus, each glass slide produces 4.3 ± 0.5 fmol of CSS nanoassemblies. The number density of CSS nanoassemblies can be controlled by the immersion time of glass slides in a Core AuNP solution and/or the concentration of the AuNP soluiton in Step (2). A close inspection of the individual CSS structures reveals that each Core AuNP houses 5–7 Sat1 AuNPs, and each Sat1 AuNP is decorated by three Sat2 AuNPs. The number of satellite AuNPs is determined by the interplay between the available space into which the AuNPs can fit and the electrostatic repulsion between the approaching AuNPs that are all negatively charged. The large difference in size between the Core (70 nm) and Sat1 (32 nm) allows more Sat1 AuNPs to attach to the Core than Sat2 AuNPs (20 nm) to Sat1 AuNPs (32 nm).

Fig. 2b displays the colors of the Core AuNP, CS, and CSS nanoassemblies prepared on glass slides. The glass slide containing the Core AuNPs exhibits a red color, but its color changes to purple and blue when Sat1 and Sat2 AuNPs, respectively, are added sequentially. The optical response in Fig. 2c is consistent with the observed color change. An extinction peak is visible at 544 nm in the UV-vis spectrum for the Core AuNPs (70 nm), rendering the adsorbed glass slide red. This peak is attributed to the well-known localized surface plasmon resonance (LSPR) of AuNPs.[2,73] An additional peak appears at 709 nm for the CS nanoassemblies where the Core and Sat1 AuNPs are connected by the C8DT molecules (gap distance, d = 1.3 nm).[61] For the CSS nanoassemblies, three peaks are observed. The shortest wavelength peak remains in the same position as that of the Core or CS AuNPs (λ = 545 nm), while the two long wavelength peaks (λ = 680 and 761 nm) appear to be split from the 709 nm peak of the CS (Fig. 2c).

To assign these peaks and determine the origin of the plasmon coupling in these complex assembly structures, we conducted finite-difference time-domain (FDTD) simulations. We constructed a symmetric CSS structure for the calculations (Fig. 3a). Four Sat1 AuNPs (32 nm) are placed along the Core (70 nm) meridian. Two additional Sat1 AuNPs are positioned at the equator at an azimuthal angle of ±90° from the meridian to complete the CS structure. For the CSS, three Sat2 AuNPs (20 nm) are attached to each Sat1 AuNP. All gap distances are set to 1.3 nm. A plane wave propagates from the top with a polarization parallel to the meridian.

Fig. 3b shows the calculated optical responses of the Core, CS, and CSS. Although the detailed peak positions differ slightly from those in the experiments, the overall features are fully consistent. A single peak appears at 551 nm for the Core. An additional peak is observed at 657 nm for the CS nanoassembly, whereas the other peak remains largely at the same position (547 nm) as that of the Core. For the CSS nanoassembly, the 657 nm peak is split into two peaks at 622 and 704 nm.

We calculated the charge density distribution at each resonance wavelength. Fig. 3c presents a cross-sectional view of the charge distribution along the meridian. The plasmon coupling for the CS or CSS nanoassemblies obeys the plasmon hybridization model developed by Nordlander and coworkers.[74,75] The dipole plasmon modes of the Core and Sat1 AuNPs interact with each other to form a stabilized dipole–dipole plasmon coupling mode ("*Di–Di*" in Fig. 3). This mode corresponds to the radiant mode proposed by Kuttner and coworkers.[70,76] Large Core AuNPs interact with light more strongly than the small Sat1 AuNPs do. Consequently, the plasmon induced on the Core governs the plasmons on the satellites. A large plasmon dipole mode on the Core AuNP aligns the dipole plasmons of the small Sat1 AuNPs in the radial direction. On the high-energy side, a weakly interacting, and thus less-stabilized coupling mode forms. Instead of the global dipole plasmon mode on the Core AuNP, the surface charges become localized and interact with the quadrupole plasmon modes of Sat1 AuNPs ("*Local–Quad*" coupling mode).

A similar pattern is observed for CSS nanoassemblies. The most stable plasmon coupling mode originates from the dipole–dipole interactions between the Core, Sat1, and Sat2 AuNPs ("*Di–Di–Di*" coupling mode). However, the coupling is not perfectly radial from the Core to Sat2. In this mode, the

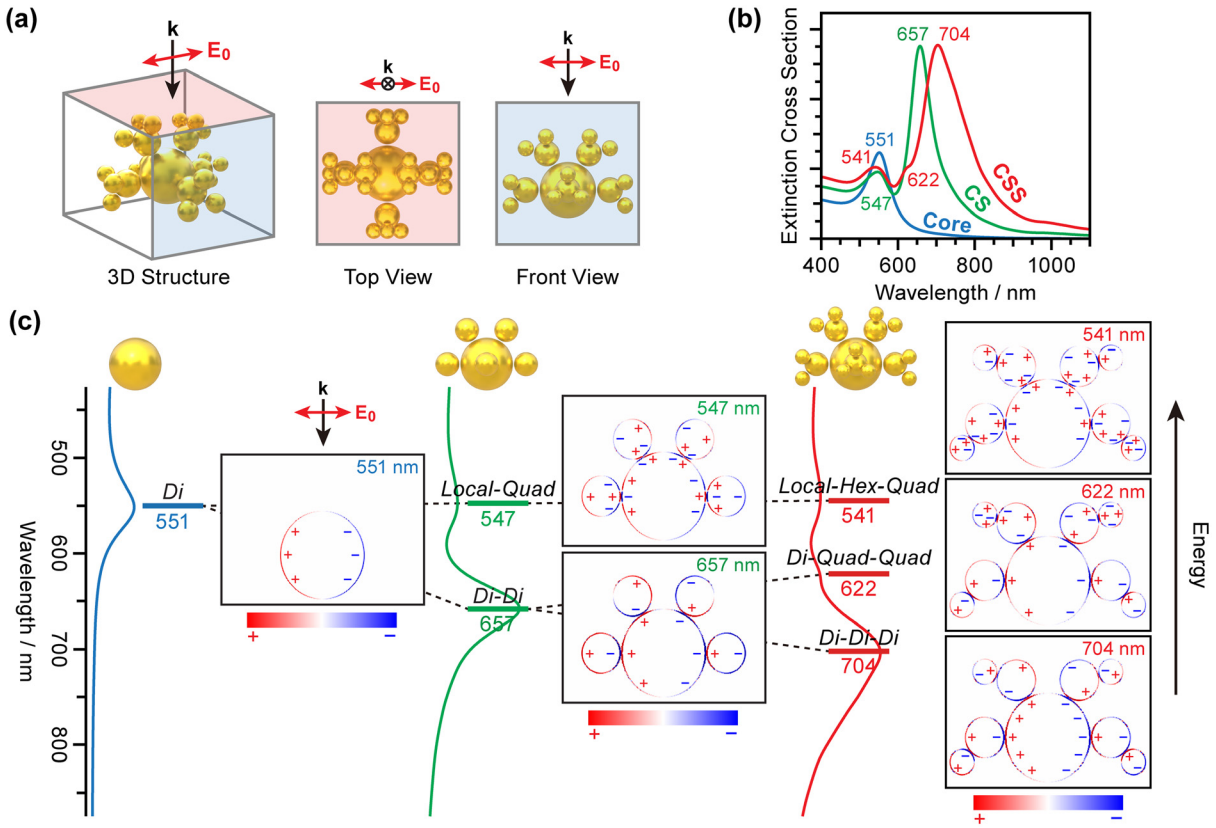

Fig. 3 Calculated optical responses of the Core, CS, and CSS nanoassemblies. (a) The CSS structure used in the calculations. ***k*** and $\boldsymbol{E_0}$ refer to the propagation and polarization of the plane wave that interacts with the CSS. (b) Calculated extinction spectra and (c) cross-sectional view of the charge density distribution at the resonance wavelengths for the Core, CS, and CSS. The plasmon coupling modes assigned from the charge density distribution are labeled at the corresponding energy levels. Dipole, quadrupole, and hexapole plasmon modes are abbreviated as *Di*, *Quad*, and *Hex*, respectively. Localized charge density interactions with their counterparts are designated as *Local*.

strong dipole plasmon of the Core AuNP influences the charge distribution of Sat1 and Sat2 at larger distances. Such a long-range interaction rotates the dipole plasmon of Sat1 and Sat2 slightly from the radial direction such that the far-side charges compensate for the plasmon dipole of the Core (Fig. S3†).

Local charge interactions play a more important role in coupling at higher energies. At 622 nm, the more polarizable quadrupole plasmon modes of Sat1 and Sat2 begin to interact with the dipole plasmon mode of the Core AuNP ("*Di–Quad–Quad*" coupling mode). Thus, *Di–Di–Di* and *Di–Quad–Quad* are the branches of the *Di–Di* mode of CS as Sat2 AuNPs are added, supporting our interpretation that the two long-wavelength peaks for CSS are the ones that split from the dipolar plasmon coupling peak of CS in the UV-vis spectra.

The *Local–Quad* mode of the CS evolves into higher-degree multipole interactions in CSS structures. Our calculations show that the interaction of the localized charge distribution of the Core with the hexapole plasmon mode of Sat1 and quadrupole plasmon mode of Sat2 creates a "*Local–Hex–Quad*" coupling mode (541 nm) whose energy is similar to the *Local–Quad* mode of CS (547 nm) and the dipole plasmon mode of the Core AuNP (551 nm).

Having found the origin of the peaks in the UV-vis spectra of CSS, we explored how these couplings change depending on the nanogap characteristics. We prepared a set of CSS nanoassemblies that comprise the same Core, Sat1, and Sat2 AuNPs, but are linked by four different combinations of C8DT and ABT linkers. Fig. 4 shows the UV-vis spectra of these CSS nanoassemblies with (Linker1–Linker2) where Linker1 and Linker2 define the nanogap between Core and Sat1 and between Sat1 and Sat2, respectively.

The three resonance peaks are consistently observed for all CSS nanoassemblies with different linkers, but the peak widths and positions vary, reflecting the difference in the coupling strengths between the AuNPs. The extinction spectrum of the CSS with the (C8DT–C8DT) linker combination exhibits three well-resolved peaks at 545, 680, and 761 nm, which are assigned to the *Local–Hex–Quad*, *Di–Quad–Quad*, and *Di–Di–Di* coupling modes, respectively (blue line). Notably, the latter two peaks of the CSS at 680 and 761 nm are split from the peak at 709 nm of the CS that is assigned to the *Di–Di* mode (dark blue line). When Linker2 uses ABT, instead of C8DT, similar split peaks are apparent but are significantly broadened (cyan line). The broadening is due to the electro-

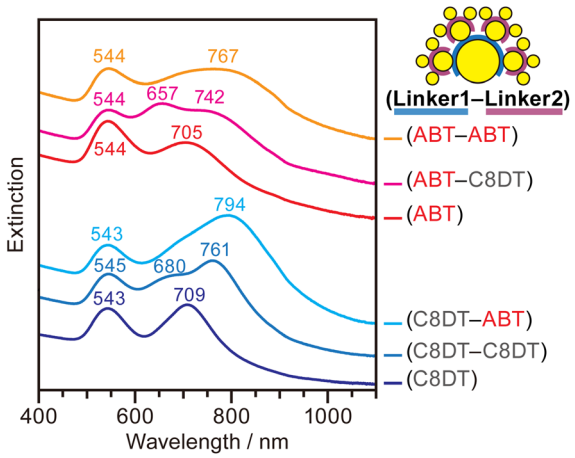

Fig. 4 UV-vis spectra of CSS with different combinations of linkers. Linker1 and Linker2 refer to the molecules used to connect Core and Sat1, and Sat1 and Sat2, respectively. For all CSS, the same types of Core (70 nm), Sat1 (32 nm), and Sat2 (20 nm) AuNPs were used. The UV-vis spectra of CS with ABT or C8DT are included for comparison. The spectra are offset for clarity.

static binding between the ABT linkers and citrates on Sat2 AuNPs. The electrostatic binding between the terminal ammonium group of ABT and carboxylates on citrate is weaker than the covalent bonding between C8DT and Sat2 where the thiol group of C8DT displaces citrates on the Sat2 AuNPs and forms an Au–S bond (Fig. S4†). Consequently, the nanogaps using ABT are less solidly defined than those formed by covalent bonding. The resulting variations in the nanogaps lead to broader coupling bands for the ABT than that for the C8DT linkers. Moreover, the *Di–Di–Di* coupling mode is more red-shifted when ABT is used as Linker2, indicating that the coupling between Sat1 and Sat2 is stronger across the nanogap formed by ABT. The molecular height of the ABT SAMs (0.9 nm) is shorter than that of C8DT SAMs (1.3 nm), which might cause stronger plasmon coupling.[61]

These features consistently appear whenever citrate-capped AuNPs are connected by ABT. The *Di–Di* coupling peak of the CS nanoassemblies connected by ABT (red line) is broader than that of the CS nanoassemblies connected by C8DT (dark blue line) in Fig. 4. When C8DT is used to attach Sat2 AuNPs to the CS with ABT, the *Di–Di* mode at 705 nm is split into two resolved peaks at 657 and 742 nm (magenta line). Comparatively, when ABT is used as Linker2 (orange line), the coupling peaks of CSS broaden and redshift. This study demonstrates that the two independently adjustable nanogaps within CSS nanoassemblies enable a control of the optical resonances in a wide wavelength range.

Electric field characteristics

Nanogaps play a major role in amplifying electric fields induced by plasmons. As two hierarchical nanogaps exist in CSS nanoassemblies, it is of great interest to compare electric fields between the first generation nanogaps ("Gap1", between Core and Sat1) and second generation nanogaps ("Gap2", between Sat1 and Sat2). SERS enables us to tackle this problem because it arises from a near-field effect that reflects the intensity of the electric fields in the nanogaps.

We prepared CS and CSS nanoassemblies on glass slides using a combination of ABT and C8DT linkers. To correlate the number of nanoassemblies and SERS intensities, we placed a finder grid (hole size = 420 × 420 μm^2, bar width = 80 μm, 50 mesh) on a glass slide and obtained the SERS spectra from the center area of a specific grid square cell using a Raman microscope (λ_{ex} = 785 nm, laser spot size = 10 μm, Fig. 5a, middle panel). The ABT molecules were used as SERS probes. The Raman scattering cross-section of the other linker (*i.e.*, C8DT) in the CSS nanoassemblies is so small, as compared to that of ABT, that only ABT vibrational peaks are observed in the SERS spectra even if both ABT and C8DT are used as linkers (Fig. S5†). This allows us to measure the electric field intensity at selected nanogaps. We compared the SERS intensity of ABT at 1586 cm^{-1} (ν_{CC} vibrational mode) when the ABT molecules were in the nanogaps of CS and CSS (Fig. 5a, left panel). Notably, the number of nanoassembly particles is another contributing factor to the SERS intensity. To account for this, we acquired the SEM images from the same grid area where we measured SERS (Fig. 5a right panel), calculated the particle density, and divided the SERS peak intensity at 1586 cm^{-1} by the number of nanoassembly particles within the laser spot size. We obtained the SERS peak intensity per nanoassembly particle from five different grid positions as described above and repeated the experiments on four or five separately prepared samples. Fig. 5b presents the average peak intensity per nanoassembly particle with one standard deviation as an error bar from these measurements.

The measured SERS intensity reflects the electric field intensity in Gap1 and Gap2, induced by plasmon excitation in the CSS nanoassembly. The results presented in Fig. 5b indicate that the Core AuNPs alone do not produce SERS signals, confirming that SERS is indeed a nanogap effect. SERS begins to occur as Sat1 AuNPs adsorb on the core AuNPs through the ABT linkers, thus consequently positioning ABT in the nanogaps between the Core and Sat1 AuNPs. The SERS intensity of a CS nanoassembly corresponds to 24. Interestingly, when Sat2 AuNPs are attached while the ABT molecules remain in Gap1, the SERS signal intensity per nanoassembly particle increases from 24 to 33 (38% increase). In other words, the SERS intensity of CSS is stronger than that of CS even if the ABT molecules experience the same nanogap environment between the Core and Sat1. This is presumably due to the increase in the scattering cross-section as the overall nanoassembly system size increases from 136 to 179 nm (32% increase).

For identical CSS structures, when the SERS probe molecules are in Gap2, the SERS intensity decreases by half compared to that when the molecules are in Gap1 (16 against 33). This finding indicates that the size of the AuNPs that define the nanogaps is important for enhancing the Raman signal. Finally, when the SERS probe molecules are in both Gap1 and Gap2, the overall SERS signal intensity is the same as the SERS

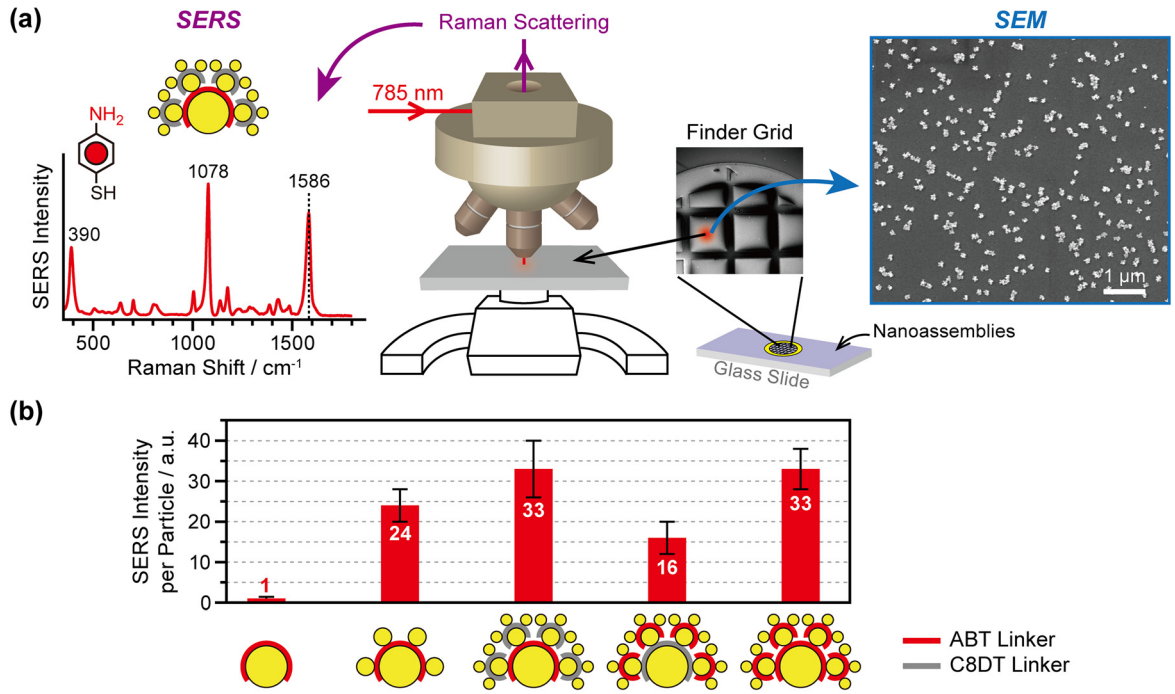

Fig. 5 Experimental measurements of electric fields from nanogaps (Gap1 and/or Gap2) using the SERS of ABT. (a) Schematic experimental setup for measuring the SERS intensity per nanoparticle (middle panel). The nanoassemblies are prepared on glass slides on which a finder grid is placed. Raman spectra of the SERS probe molecules (ABT) are acquired from one of the finder grid cells using a Raman microscope with a Raman excitation laser at 785 nm (left panel). The number of nanoassemblies probed by SERS is measured using SEM from the same cell of the finder grid (right panel). (b) SERS intensity per particle when the ABT SERS probe molecules are on the Core AuNP without satellite AuNPs, in the Gap1 of CS and CSS, in the Gap2 of CSS, and in both the Gap1 and Gap2 of CSS.

signal intensity from Gap1 alone, suggesting that the electric field intensity of Gap1 dominates that of the entire system.

We compared our experimental results with the calculations. Fig. 6a shows a cross-sectional view of the electric field distribution of the Core, CS, and CSS nanoparticles induced by

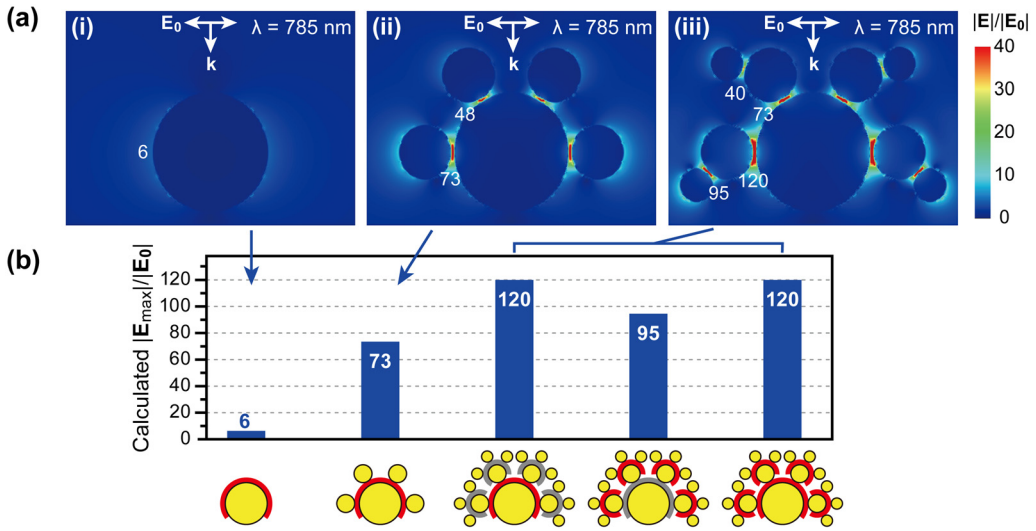

Fig. 6 Calculated electric field intensities at the nanogaps. (a) 2D cross-sectional view of the 3D electric field distribution along the meridian of the nanoparticles, induced by a 785 nm light with propagation (***k***) and polarization (E_0) indicated in the figure. The numbers refer to the magnitude of the electric fields, compared to that of incident electric fields ($|E|/|E_0|$) at each nanogap. (b) Comparison of the electric field enhancement at the nanogaps of the Core, CS, and CSS nanoassemblies. The sizes of the AuNPs are identical to those used in the experiments. The nanogaps are set as 1.3 nm, mimicking the C8DT linkers.

light at 785 nm propagating from the top with polarization, labeled $\boldsymbol{E_0}$. For comparison of the electric fields between Gap1 and Gap2, we used the same gap distance, 1.3 nm, for both nanogaps. The numbers in the figure represent the magnitude of the induced electric field compared to that of the incident electric field ($|\boldsymbol{E}|/|\boldsymbol{E_0}|$) at each nanogap. Note that the fourth power of the ratio determines the SERS enhancement factor.[13]

The general trend in the calculated electric field enhancement for each nanoassembly structure is consistent with our observation of the SERS signal intensity. The electric field around the single Core AuNP is weakly enhanced, yielding a $|\boldsymbol{E}|/|\boldsymbol{E_0}|$ of only 6. Such a weak electric field enhancement on an individual AuNP agrees with our experimental observation in Fig. 5. The electric field is significantly enhanced only in the nanogaps. Upon the adsorption of Sat1 AuNPs (*i.e.*, CS nanoassembly), the electric field enhancement at the same position considerably increases from 6 to 73 (Fig. 6a(ii)).

Interestingly, the molecule in the nanogap between Core and Sat1 experiences a significantly greater electric field in the CSS than in the CS. Fig. 6 shows that the electric field in Gap1 increases from 73 to 120 (64% increase) or 48 to 73 (52% increase) as Sat2 AuNPs attach to Sat1. The presence of Sat2 AuNPs seems to enhance the electric field in the area where Sat2 is not directly associated. This calculation result correlates with the experiments. The SERS signal intensity from Gap1 increases from 24 to 33 as Sat2 AuNPs attach to Sat1 (Fig. 5).

Further calculations reveal that this effect is attributed to the excitation intensity that is used to induce electric fields. As the excitation wavelengths are closer to the plasmon resonance of nanoparticles, a stronger electric field is induced. At 785 nm, CSS has a larger scattering cross-section (1.25×10^{-14} m^2) than CS (0.41×10^{-14} m^2) (Fig. S6†). Consequently, an overall stronger electric field is induced in CSS than in CS, as shown in Fig. 6. In contrast, excitation of the CS and CSS at their resonance wavelengths results in a higher electric field intensity for CS ($|\boldsymbol{E_{max}}|/|\boldsymbol{E_0}|$ = 243) than for CSS ($|\boldsymbol{E_{max}}|/|\boldsymbol{E_0}|$ = 192), which is consistent with the larger scattering cross-section of CS than that of CSS at each resonance wavelength (Fig. S6†).

Finally, we compared the electric field enhancement between Gap1 and Gap2 within the same CSS. The calculations show that the electric field at Gap2 is weaker than that at Gap1 (95 against 120 or 40 against 73). This is also qualitatively consistent with the gap-selective SERS measurement results presented in Fig. 5. The SERS intensity in CSS at Gap2 is weaker than that at Gap1 in CSS (16 against 33).

The electric field intensity at each nanogap in CSS ranges from 40 to 120; the largest enhancement is observed at Gap1 when the Core and Sat1 AuNPs are aligned in the polarization direction of the light. Our experimental results suggest that such an electric field enhancement dominates the SERS signal. The contribution from the other nanogaps is small or negligible. Our study provides a method for the assembly of hierarchical plasmonic nanostructures and a guide for the smart design of SERS probe materials.

Conclusions

We successfully constructed CSS hierarchical nanoassembly structures. The sequential assembly of 70, 32, and 20 nm AuNPs on glass slides using ABT, C8DT, or BDMT linkers leads to the formation of CSS nanoassemblies with ultrahigh purity. Each CSS nanoassembly consists of 5–7 Sat1 AuNPs surrounding a Core AuNP, and each Sat1 is covered with three Sat2 AuNPs. UV-vis spectra show the evolution of the plasmon coupling peaks as Sat1 and Sat2 AuNPs are added to the Core AuNP. CS displays a plasmon coupling mode peak (~710 nm) in the longer wavelength region in addition to the peak (~540 nm) near the typical LSPR band of individual AuNPs. The long wavelength peak splits into two peaks at ~680 and ~760 nm upon the formation of CSS. Charge density distribution calculations reveal that the three peaks in the CSS nanoassembly are assigned to the *Di–Di–Di*, *Di–Quad–Quad*, and *Local–Hex–Quad* coupling modes from right to left in the spectrum. The peak widths are related to the variations in the nanogap distances, which are determined by the binding characteristics between the linker and AuNP surfaces. The plasmon-induced electric field amplification at Gap1 and Gap2 is measured using SERS by positioning the ABT molecules in the desired nanogaps. SERS signals cannot be observed without the nanogaps. The SERS signal intensity from Gap1, between the Core and Sat1 AuNPs in the CS nanoassemblies, increases by 38% upon adsorption of Sat2 AuNPs. The Raman enhancement from Gap2 is approximately half of that from Gap1. Positioning the Raman probe molecules in both Gap1 and Gap2 yields a SERS signal intensity which is approximately the same as that when the molecules are only in Gap1. The electric field intensity calculated using the FDTD method is consistent with our experimental observations. This new type of nanostructure provides more flexibility to control and enhance the plasmonic properties of noble metal nanoparticles.

Conflicts of interest

There are no conflicts to declare.

Acknowledgements

This work was supported by the National Research Foundation (NRF) of Korea (Grant No. 2019R1A2C1084078 and 2020R1A5A1018052). J. P. acknowledges support from the Chung-Ang University Graduate Research Scholarship (2021).

References

1 M. Rycenga, C. M. Cobley, J. Zeng, W. Li, C. H. Moran, Q. Zhang, D. Qin and Y. Xia, Controlling the Synthesis and Assembly of Silver Nanostructures for Plasmonic Applications, *Chem. Rev.*, 2011, **111**, 3669–3712.

2 M.-C. Daniel and D. Astruc, Gold Nanoparticles: Assembly, Supramolecular Chemistry, Quantum-Size-Related Properties, and Applications toward Biology, Catalysis, and Nanotechnology, *Chem. Rev.*, 2004, **104**, 293–346.
3 P. K. Jain, X. Huang, I. H. El-Sayed and M. A. El-Sayed, Noble Metals on the Nanoscale: Optical and Photothermal Properties and Some Applications in Imaging, Sensing, Biology, and Medicine, *Acc. Chem. Res.*, 2008, **41**, 1578–1586.
4 T. W. Odom and G. C. Schatz, Introduction to Plasmonics, *Chem. Rev.*, 2011, **111**, 3667–3668.
5 S. A. Maier, *Plasmonics: Fundamentals and Applications*, Springer, New York, 2007.
6 W. Ma, M. Sun, L. Xu, L. Wang, H. Kuang and C. Xu, A SERS Active Gold Nanostar Dimer for Mercury Ion Detection, *Chem. Commun.*, 2013, **49**, 4989–4991.
7 A. Eshkeiti, B. B. Narakathu, A. S. G. Reddy, A. Moorthi, M. Z. Atashbar, E. Rebrosova, M. Rebros and M. Joyce, Detection of Heavy Metal Compounds Using a Novel Inkjet Printed Surface Enhanced Raman Spectroscopy (SERS) Substrate, *Sens. Actuators, B*, 2012, **171**, 705–711.
8 C. Byram, S. S. B. Moram and V. R. Soma, SERS Based Detection of Multiple Analytes from Dye/Explosive Mixtures Using Picosecond Laser Fabricated Gold Nanoparticles and Nanostructures, *Analyst*, 2019, **144**, 2327–2336.
9 T. Liyanage, A. Rael, S. Shaffer, S. Zaidi, J. V. Goodpaster and R. Sardar, Fabrication of a Self-Assembled and Flexible SERS Nanosensor for Explosive Detection at Parts-Per-Quadrillion Levels from Fingerprints, *Analyst*, 2018, **143**, 2012–2022.
10 M. E. Stewart, C. R. Anderton, L. B. Thompson, J. Maria, S. K. Gray, J. A. Rogers and R. G. Nuzzo, Nanostructured Plasmonic Sensors, *Chem. Rev.*, 2008, **108**, 494–521.
11 X. Huang, I. H. El-Sayed, W. Qian and M. A. El-Sayed, Cancer Cell Imaging and Photothermal Therapy in the near-Infrared Region by Using Gold Nanorods, *J. Am. Chem. Soc.*, 2006, **128**, 2115–2120.
12 N. H. Ly, H. H. Kim and S.-W. Joo, On-Site Detection for Hazardous Materials in Chemical Accidents, *Bull. Korean Chem. Soc.*, 2021, **42**, 4–16.
13 E. C. Le Ru and P. G. Etchegoin, *Principles of Surface-Enhanced Raman Spectroscopy and Related Plasmonic Effects*, Elsevier, Oxford, U.K., 2009.
14 H.-H. Shin, J.-J. Koo, K. S. Lee and Z. H. Kim, Chemical Reactions Driven by Plasmon-Induced Hot Carriers, *Appl. Mater. Today*, 2019, **16**, 112–119.
15 Y. Zhang, S. He, W. Guo, Y. Hu, J. Huang, J. R. Mulcahy and W. D. Wei, Surface-Plasmon-Driven Hot Electron Photochemistry, *Chem. Rev.*, 2018, **118**, 2927–2954.
16 M. G. Walter, E. L. Warren, J. R. McKone, S. W. Boettcher, Q. Mi, E. A. Santori and N. S. Lewis, Solar Water Splitting Cells, *Chem. Rev.*, 2010, **110**, 6446–6473.
17 J. S. DuChene, G. Tagliabue, A. J. Welch, W.-H. Cheng and H. A. Atwater, Hot Hole Collection and Photoelectrochemical CO_2 Reduction with Plasmonic Au/P-GaN Photocathodes, *Nano Lett.*, 2018, **18**, 2545–2550.
18 Q. Cao and R. C. Che, Tailoring Au-Ag-S Composite Microstructures in One-Pot for Both SERS Detection and Photocatalytic Degradation of Plasticizers DEHA and DEHP, *ACS Appl. Mater. Interfaces*, 2014, **6**, 7020–7027.
19 J. Lee, S. Mubeen, X. L. Ji, G. D. Stucky and M. Moskovits, Plasmonic Photoanodes for Solar Water Splitting with Visible Light, *Nano Lett.*, 2012, **12**, 5014–5019.
20 Z. J. Coppens, W. Li, D. G. Walker and J. G. Valentine, Probing and Controlling Photothermal Heat Generation in Plasmonic Nanostructures, *Nano Lett.*, 2013, **13**, 1023–1028.
21 H. Chen, L. Shao, T. Ming, Z. Sun, C. Zhao, B. Yang and J. Wang, Understanding the Photothermal Conversion Efficiency of Gold Nanocrystals, *Small*, 2010, **6**, 2272–2280.
22 M. N. Biutty, M. Zakia and S. I. Yoo, Enhanced Photothermal Heating from One-Dimensional Assemblies of Au Nanoparticles Encapsulated by TiO_2 Shell, *Bull. Korean Chem. Soc.*, 2020, **41**, 1033–1039.
23 J. M. Stern, J. Stanfield, W. Kabbani, J. T. Hsieh and J. R. A. Cadeddu, Selective Prostate Cancer Thermal Ablation with Laser Activated Gold Nanoshells, *J. Urol.*, 2008, **179**, 748–753.
24 L. Jauffred, A. Samadi, H. Klingberg, P. M. Bendix and L. B. Oddershede, Plasmonic Heating of Nanostructures, *Chem. Rev.*, 2019, **119**, 8087–8130.
25 P. K. Jain, W. Huang and M. A. El-Sayed, On the Universal Scaling Behavior of the Distance Decay of Plasmon Coupling in Metal Nanoparticle Pairs: A Plasmon Ruler Equation, *Nano Lett.*, 2007, **7**, 2080–2088.
26 C. Sönnichsen, B. M. Reinhard, J. Liphardt and A. P. Alivisatos, A Molecular Ruler Based on Plasmon Coupling of Single Gold and Silver Nanoparticles, *Nat. Biotechnol.*, 2005, **23**, 741–745.
27 L. Yang, H. Wang, B. Yan and B. M. Reinhard, Calibration of Silver Plasmon Rulers in the 1–25 nm Separation Range: Experimental Indications of Distinct Plasmon Coupling Regimes, *J. Phys. Chem. C*, 2010, **114**, 4901–4908.
28 E. Hao and G. C. Schatz, Electromagnetic Fields around Silver Nanoparticles and Dimers, *J. Chem. Phys.*, 2004, **120**, 357–366.
29 J. B. Lassiter, J. Aizpurua, L. I. Hernandez, D. W. Brandl, I. Romero, S. Lal, J. H. Hafner, P. Nordlander and N. J. Halas, Close Encounters between Two Nanoshells, *Nano Lett.*, 2008, **8**, 1212–1218.
30 J. Langer, D. J. D. Aberasturi, J. Aizpurua, R. A. Alvarez-Puebla, B. Auguié, J. J. Baumberg, G. C. Bazan, S. E. J. Bell, A. Boisen, A. G. Brolo, J. Choo, D. Cialla-May, V. Deckert, L. Fabris, K. Faulds, F. J. G. D. Abajo, R. Goodacre, D. Graham, A. J. Haes, C. L. Haynes, C. Huck, T. Itoh, M. Käll, J. Kneipp, N. A. Kotov, H. Kuang, E. C. L. Ru, H. K. Lee, J.-F. Li, X. Y. Ling, S. A. Maier, T. Mayerhöfer, M. Moskovits, K. Murakoshi, J.-M. Nam, S. Nie, Y. Ozaki, I. Pastoriza-Santos, J. Perez-Juste, J. Popp, A. Pucci, S. Reich, B. Ren, G. C. Schatz, T. Shegai, S. Schlücker, L.-L. Tay, K. G. Thomas, Z.-Q. Tian, R. P. V. Duyne, T. Vo-Dinh, Y. Wang, K. A. Willets, C. Xu, H. Xu, Y. Xu,

Y. S. Yamamoto, B. Zhao and L. M. Liz-Marzán, Present and Future of Surface-Enhanced Raman Scattering, *ACS Nano*, 2019, **14**, 28–117.

31 S. Schlücker, Surface-Enhanced Raman Spectroscopy: Concepts and Chemical Applications, *Angew. Chem., Int. Ed.*, 2014, **53**, 4756–4795.

32 L. V. Besteiro and A. O. Govorov, Amplified Generation of Hot Electrons and Quantum Surface Effects in Nanoparticle Dimers with Plasmonic Hot Spots, *J. Phys. Chem. C*, 2016, **120**, 19329–19339.

33 H. Harutyunyan, A. B. Martinson, D. Rosenmann, L. K. Khorashad, L. V. Besteiro, A. O. Govorov and G. P. Wiederrecht, Anomalous Ultrafast Dynamics of Hot Plasmonic Electrons in Nanostructures with Hot Spots, *Nat. Nanotechnol.*, 2015, **10**, 770.

34 S. Mukherjee, F. Libisch, N. Large, O. Neumann, L. V. Brown, J. Cheng, J. B. Lassiter, E. A. Carter, P. Nordlander and N. J. Halas, Hot Electrons Do the Impossible: Plasmon-Induced Dissociation of H_2 on Au, *Nano Lett.*, 2013, **13**, 240–247.

35 H. Huh, H. D. Trinh, D. Lee and S. Yoon, How Does a Plasmon-Induced Hot Charge Carrier Break a C–C Bond?, *ACS Appl. Mater. Interfaces*, 2019, **11**, 24715–24724.

36 L. T. M. Huynh, S. Kim and S. Yoon, Effect of Material and Shape of Nanoparticles on Hot Carrier Generation, *ACS Photonics*, 2022, **9**, 3260–3267.

37 D. Kumar, J. Y. Lee, M. J. Moon, W. Kim, Y. Y. Jeong, C. H. Park and C. S. Kim, Nanogap-Containing Thermo-Plasmonic Nano-Heaters for Amplified Photo-Triggered Tumor Ablation at Low Laser Power Density, *Biomater. Sci.*, 2022, **10**, 2394–2408.

38 H. Cha, J. H. Yoon and S. Yoon, Probing Quantum Plasmon Coupling Using Gold Nanoparticle Dimers with Tunable Interparticle Distances Down to the Subnanometer Range, *ACS Nano*, 2014, **8**, 8554–8563.

39 A. P. Alivisatos, K. P. Johnsson, X. Peng, T. E. Wilson, C. J. Loweth, M. P. Bruchez and P. G. Schultz, Organization of 'Nanocrystal Molecules' Using DNA, *Nature*, 1996, **382**, 609–611.

40 H. Wang and B. M. Reinhard, Monitoring Simultaneous Distance and Orientation Changes in Discrete Dimers of DNA Linked Gold Nanoparticles, *J. Phys. Chem. C*, 2009, **113**, 11215–11222.

41 M. P. Busson, B. Rolly, B. Stout, N. Bonod, E. Larquet, A. Polman and S. Bidault, Optical and Topological Characterization of Gold Nanoparticle Dimers Linked by a Single DNA Double Strand, *Nano Lett.*, 2011, **11**, 5060–5065.

42 C. Chi, F. Vargas-Lara, A. V. Tkachenko, F. W. Starr and O. Gang, Internal Structure of Nanoparticle Dimers Linked by DNA, *ACS Nano*, 2012, **6**, 6793–6802.

43 X. Lan, Z. Chen, B.-J. Liu, B. Ren, J. Henzie and Q. Wang, DNA-Directed Gold Nanodimers with Tunable Sizes and Interparticle Distances and Their Surface Plasmonic Properties, *Small*, 2013, **9**, 2308–2315.

44 L. C. Brousseau, J. P. Novak, S. M. Marinakos and D. L. Feldheim, Assembly of Phenylacetylene-Bridged Gold Nanocluster Dimers and Trimers, *Adv. Mater.*, 1999, **11**, 447–449.

45 G. Chen, Y. Wang, M. Yang, J. Xu, S. J. Goh, M. Pan and H. Chen, Measuring Ensemble-Averaged Surface-Enhanced Raman Scattering in the Hotspots of Colloidal Nanoparticle Dimers and Trimers, *J. Am. Chem. Soc.*, 2010, **132**, 3644–3645.

46 M. M. Maye, M. T. Kumara, D. Nykypanchuk, W. B. Sherman and O. Gang, Switching Binary States of Nanoparticle Superlattices and Dimer Clusters by DNA Strands, *Nat. Nanotechnol.*, 2010, **5**, 116–120.

47 D. Lee and S. Yoon, Gold Nanotrimers: A Preparation Method and Optical Responses, *Bull. Korean Chem. Soc.*, 2016, **37**, 987–988.

48 L. Chuntonov and G. Haran, Trimeric Plasmonic Molecules: The Role of Symmetry, *Nano Lett.*, 2011, **11**, 2440–2445.

49 S. J. Barrow, S. M. Collins, D. Rossouw, A. M. Funston, G. A. Botton, P. A. Midgley and P. Mulvaney, Electron Energy Loss Spectroscopy Investigation into Symmetry in Gold Trimer and Tetramer Plasmonic Nanoparticle Structures, *ACS Nano*, 2016, **10**, 8552–8563.

50 H. Lee, G.-H. Kim, J.-H. Lee, N. H. Kim, J.-M. Nam and Y. D. Suh, Quantitative Plasmon Mode and Surface-Enhanced Raman Scattering Analyses of Strongly Coupled Plasmonic Nanotrimers with Diverse Geometries, *Nano Lett.*, 2015, **15**, 4628–4636.

51 D. Steinigeweg, M. Schütz and S. Schlücker, Single Gold Trimers and 3D Superstructures Exhibit a Polarization-Independent SERS Response, *Nanoscale*, 2013, **5**, 110–113.

52 R. Watanabe-Tamaki, A. Ishikawa, T. Tanaka, T. Zako and M. Maeda, DNA-Templating Mass Production of Gold Trimer Rings for Optical Metamaterials, *J. Phys. Chem. C*, 2012, **116**, 15028–15033.

53 T. Shegai, Z. Li, T. Dadosh, Z. Zhang, H. Xu and G. Haran, Managing Light Polarization Via Plasmon-Molecule Interactions within an Asymmetric Metal Nanoparticle Trimer, *Proc. Natl. Acad. Sci. U. S. A.*, 2008, **105**, 16448–16453.

54 X. Shen, A. Asenjo-Garcia, Q. Liu, Q. Jiang, F. J. García de Abajo, N. Liu and B. Ding, Three-Dimensional Plasmonic Chiral Tetramers Assembled by DNA Origami, *Nano Lett.*, 2013, **13**, 2128–2133.

55 N. Pazos-Perez, C. S. Wagner, J. M. Romo-Herrera, L. M. Liz-Marzán, G. d. Abajo, F. J. Wittemann, A. Fery, A. Alvarez-Puebla and R. A, Organized Plasmonic Clusters with High Coordination Number and Extraordinary Enhancement in Surface-Enhanced Raman Scattering (SERS), *Angew. Chem., Int. Ed.*, 2012, **51**, 12688–12693.

56 M. Wang, M. Cao, Z. Guo and N. Gu, Two-Step Decomposition of Plasmon Coupling in Plasmonic Oligomers, *J. Phys. Chem. C*, 2013, **117**, 11713–11717.

57 T. Chen, M. Pourmand, A. Feizpour, B. Cushman and B. M. Reinhard, Tailoring Plasmon Coupling in Self-Assembled One-Dimensional Au Nanoparticle Chains

through Simultaneous Control of Size and Gap Separation, *J. Phys. Chem. Lett.*, 2013, **4**, 2147–2152.

58 S. J. Barrow, A. M. Funston, D. E. Gomez, T. J. Davis and P. Mulvaney, Surface Plasmon Resonances in Strongly Coupled Gold Nanosphere Chains from Monomer to Hexamer, *Nano Lett.*, 2011, **11**, 4180–4187.

59 Y. Wang, G. Chen, M. Yang, G. Silber, S. Xing, L. H. Tan, F. Wang, Y. Feng, X. Liu, S. Li and H. Chen, A Systems Approach Towards the Stoichiometry-Controlled Hetero-Assembly of Nanoparticles, *Nat. Commun.*, 2010, **1**, 87.

60 J. M. Romo-Herrera, R. A. Alvarez-Puebla and L. M. Liz-Marzán, Controlled Assembly of Plasmonic Colloidal Nanoparticle Clusters, *Nanoscale*, 2011, **3**, 1304–1315.

61 J. H. Yoon, J. Lim and S. Yoon, Controlled Assembly and Plasmonic Properties of Asymmetric Core-Satellite Nanoassemblies, *ACS Nano*, 2012, **6**, 7199–7208.

62 J. H. Yoon and S. Yoon, Probing Interfacial Interactions Using Core-Satellite Plasmon Rulers, *Langmuir*, 2013, **29**, 14772–14778.

63 W. Xie, B. Walkenfort and S. Schlücker, Label-Free SERS Monitoring of Chemical Reactions Catalyzed by Small Gold Nanoparticles Using 3D Plasmonic Superstructures, *J. Am. Chem. Soc.*, 2013, **135**, 1657–1660.

64 J. H. Yoon, Y. Zhou, M. G. Blaber, G. C. Schatz and S. Yoon, Surface Plasmon Coupling of Compositionally Heterogeneous Core-Satellite Nanoassemblies, *J. Phys. Chem. Lett.*, 2013, **4**, 1371–1378.

65 D. Rodriguez-Fernandez, J. Langer, M. Henriksen-Lacey and L. M. Liz-Marzan, Hybrid Au-SiO_2 Core-Satellite Colloids as Switchable SERS Tags, *Chem. Mater.*, 2015, **27**, 2540–2545.

66 D. S. Sebba and A. A. Lazarides, Robust Detection of Plasmon Coupling in Core-Satellite Nanoassemblies Linked by DNA, *J. Phys. Chem. C*, 2008, **112**, 18331–18339.

67 D. S. Sebba, J. J. Mock, D. R. Smith, T. H. LaBean and A. A. Lazarides, Reconfigurable Core-Satellite Nanoassemblies as Molecularly-Driven Plasmonic Switches, *Nano Lett.*, 2008, **8**, 1803–1808.

68 S. Pal, J. Sharma, H. Yan and Y. Liu, Stable Silver Nanoparticle-DNA Conjugates for Directed Self-Assembly of Core-Satellite Silver-Gold Nanoclusters, *Chem. Commun.*, 2009, 6059–6061.

69 M. Schutz and S. Schlucker, Molecularly Linked 3D Plasmonic Nanoparticle Core/Satellite Assemblies: SERS Nanotags with Single-Particle Raman Sensitivity, *Phys. Chem. Chem. Phys.*, 2015, **17**, 24356–24360.

70 R. P. M. Höller, M. Dulle, S. Thomä, M. Mayer, A. M. Steiner, S. Förster, A. Fery, C. Kuttner and M. Chanana, Protein-Assisted Assembly of Modular 3D Plasmonic Raspberry-Like Core/Satellite Nanoclusters: Correlation of Structure and Optical Properties, *ACS Nano*, 2016, **10**, 5740–5750.

71 N. Pazos-Perez, J. M. Fitzgerald, V. Giannini, L. Guerrini and R. A. Alvarez-Puebla, Modular Assembly of Plasmonic Core–Satellite Structures as Highly Brilliant SERS-Encoded Nanoparticles, *Nanoscale Adv.*, 2019, **1**, 122–131.

72 J. C. Love, L. A. Estroff, J. K. Kriebel, R. G. Nuzzo and G. M. Whitesides, Self-Assembled Monolayers of Thiolates on Metals as a Form of Nanotechnology, *Chem. Rev.*, 2005, **105**, 1103–1170.

73 P. K. Jain, K. S. Lee, I. H. El-Sayed and M. A. El-Sayed, Calculated Absorption and Scattering Properties of Gold Nanoparticles of Different Size, Shape, and Composition: Applications in Biological Imaging and Biomedicine, *J. Phys. Chem. B*, 2006, **110**, 7238–7248.

74 E. Prodan, C. Radloff, N. J. Halas and P. Nordlander, A Hybridization Model for the Plasmon Response of Complex Nanostructures, *Science*, 2003, **302**, 419–422.

75 P. Nordlander, C. Oubre, E. Prodan, K. Li and M. I. Stockman, Plasmon Hybridization in Nanoparticle Dimers, *Nano Lett.*, 2004, **4**, 899–903.

76 R. P. M. Höller, I. J. Jahn, D. Cialla-May, M. Chanana, J. Popp, A. Fery and C. Kuttner, Biomacromolecular-Assembled Nanoclusters: Key Aspects for Robust Colloidal SERS Sensing, *ACS Appl. Mater. Interfaces*, 2020, **12**, 57302–57313.

